Pergamon

Int. J. Heat Mass Transfer. Vol. 39, No. 2, pp. 247–257, 1996

0017-9310/96 $9.50+0.00

0017-9310(95)00137-9

Thermocapillary flow effects on convective droplet evaporation

ANN T. SHIH and CONSTANTINE M. MEGARIDIS†

Department of Mechanical Engineering, University of Illinois at Chicago, Chicago, IL 60607-7022, U.S.A.

(*Received* 18 *May* 1994 *and in final form* 15 *March* 1995)

Abstract—The thermocapillary convection effect on the dynamic behavior of a vaporizing–convecting hydrocarbon droplet is investigated numerically in a laminar, axisymmetric environment. The model predicts that surface-tension gradients along the gas–liquid interface strengthen droplet internal circulation and result in shorter evaporation lifetimes. The relative effect of thermocapillary stresses on overall droplet evaporation rates is nearly independent of Reynolds number. While Nusselt numbers on the droplet surface are little affected, a significant reduction of drag coefficient is observed when thermocapillary convection is taken into account. A substantial enhancement of the corresponding Sherwood numbers is also predicted. The results indicate that the Marangoni stresses cause temporal flow oscillations along the droplet interface at early stages of the droplet evaporation lifetime.

INTRODUCTION

Fuel spray processes are critical to a plethora of industrial applications. Power generation in furnaces, gas turbine combustors and internal combustion engines, are only a few technologies incorporating evaporating sprays. Due to the importance of the relevant spray dynamical processes, intensive effort has been put forth to understand the fundamental mechanisms governing the evaporation and combustion of liquid fuel droplets. The extensive literature reviews by Law [1], Faeth [2], Dwyer [3] and Sirignano [4, 5] attest to the abundance of investigations analyzing droplet evaporation and combustion phenomena. The majority of the conducted research has been devoted to understanding the mechanisms that enhance droplet evaporation–combustion so as to ultimately increase combustion efficiency.

A variety of detailed models has been developed over the past decade, addressing transient heating and evaporation of isolated fuel droplets exposed to high-temperature, laminar, convective environments [6]–[11]. These models have provided significant insight into the fundamental transport mechanisms of convective droplet evaporation. It is worth noting, however, that effects of surface-tension gradients because of variations in interfacial temperature (Marangoni effect) have been generally neglected. In that respect, the viscous stresses on the droplet surface have been generally assumed to be dominant over surface tension gradients. A recent study by Lozinski and Matalon [12] has considered the Marangoni effect on the internal circulation of a spinning droplet, in the limit of small Reynolds and Marangoni numbers, but did not report on its effect on liquid evaporation rates. Haywood *et al.* [13] presented an axisymmetric model that considered both transient deformation and surface tension effects on convective droplet evaporation. However, the isolated effect of the Marangoni stresses was not examined due to the simultaneous consideration of droplet deformation. Finally, Niazmand *et al.* [14] employed a finite volume formulation and presented some preliminary results on the importance of Marangoni convection in single component droplet vaporization. The same authors used an order-of-magnitude calculation to demonstrate the occasional significance of capillary effects on droplet evaporation dynamics. In summary, recent studies have indicated that surface-tension gradients generate thermocapillary convection that under certain conditions might not be negligible compared to the shear-induced internal flow. To this end, thermocapillary motion effects may have a substantial influence on droplet evaporation characteristics.

The current study targets the impact of thermocapillary motion on a spherical droplet vaporizing at elevated pressures (being typical of a gas turbine combustor environment). The Marangoni effect on transient fluid dynamics, as well as on heat and mass transport between the ambient fluid and the vaporizing droplet is discussed in detail. The numerical calculations presented herein are based on the computational model of Chiang *et al.* [11] which was developed for an isolated, single-component droplet vaporizing in a high-temperature convective environment ($Re \sim 100$).

MODEL DESCRIPTION AND ANALYSIS

The droplet configuration considered herein is identical to that modeled by Chiang *et al.* [11], and

† Author to whom correspondence should be addressed.

NOMENCLATURE

a	instantaneous droplet radius
C_d	drag coefficient
d	instantaneous droplet diameter
f_C	computed oscillation frequency
Ma	Marangoni number, $\gamma T_\infty/(U_\infty \mu_\infty)$
n	normal coordinate
p	pressure
Re	gas-phase Reynolds number, $U_\infty d\rho_\infty/\mu_\infty$
t	time
T	temperature
U_∞	free-stream velocity
V	velocity component
We	Weber number, $\rho_\infty U_\infty^2 d/\sigma$.

Greek symbols

γ	$-\mathrm{d}\sigma/\mathrm{d}T$
θ	tangential coordinate
μ	dynamic viscosity
ρ	density
σ	surface tension coefficient
τ	viscous shear stress
τ_{Hg}	gas-phase hydrodynamic diffusion time, $t\mu_\infty/(a_0^2\rho_\infty)$.

Subscripts

g	gas phase
l	liquid phase
n	radial (normal) direction
θ	tangential direction
0	initial condition (t = 0)
∞	free-stream condition.

Superscript

*	non-dimensional quantity.

involves a spherical, pure-fuel droplet containing a quiescent liquid at uniform temperature before it is injected into a parallel hot-gas stream. The above flow is assumed to be laminar and axisymmetric. Immediately after exposure to the ambient flow and as a result of the induced drag force, the droplet is accelerated in the direction of the gaseous stream. Thus, the relative velocity between the ambient stream and the droplet is reduced with time. In addition, the evaporation of liquid mass gradually reduces the droplet size. Therefore, the relevant Reynolds number based on relative velocity between droplet and free stream follows a monotonically decreasing trend with time. The range of flow Reynolds numbers considered is 10–100, as applicable to most practical spray combustion applications [5]. The model assumes the droplet to remain spherical at all times, and considers variable thermophysical properties (except densities, heat capacities and thermal conductivities for the liquid), as well as transient heating with internal liquid circulation.

The basic assumptions of the model, along with the complete set of governing equations and associated boundary conditions are elaborately described in [11]. In brief, the gas phase was described by the continuity equation, the axial and radial components of the momentum equation, the energy equation, and finally, the species equation. The liquid phase was described by the energy equation, and a vorticity-stream function formulation to circumvent the pressure calculation in the droplet interior. Conditions across the liquid–gas interface included continuity of shear stress, heat and mass flux, tangential velocity, temperature, and the assumption of phase equilibrium. A modification introduced in the current work involved the convective terms in the liquid-phase energy equation, which were discretized by a hybrid first-order upwind differencing scheme. This scheme was found [15] to provide more accurate predictions when compared to central differencing. Furthermore, the tangential surface-tension gradient term has been incorporated in the balance of the viscous shear stresses on the droplet surface, i.e.

$$\tau_l = \tau_g + (\nabla\sigma)_\theta \tag{1}$$

where τ_l and τ_g denote shear stress on the liquid and gas side, respectively. It is noted that the thermocapillary stress tends to drive the liquid from hot to cold regions of the gas–liquid interface. Using spherical coordinates (radial: n, tangential: θ), the shear stress τ on either side of the droplet interface is defined by

$$\tau_i = \mu_i\left[\frac{\partial V_\theta}{\partial n} - \frac{V_\theta}{a} + \frac{1}{a}\frac{\partial V_n}{\partial \theta}\right]_i \tag{2}$$

where the subscript i indicates the specific phase (g for gas, l for liquid), μ_i the dynamic viscosity, V the velocity and a the instantaneous droplet radius.

The surface tension coefficient σ for a pure fluid is a property that varies with temperature; $\sigma(T)$. For most common fluids, the temperature dependence of σ is linear [16]; $\mathrm{d}\sigma/\mathrm{d}T$ = constant. In general, the surface tension coefficient decreases with rising liquid temperature, i.e. $\mathrm{d}\sigma/\mathrm{d}T = -\gamma < 0$. A constant value of $\gamma = 10^{-4}$ N m^{-1}K^{-1} has been used in this study, being representative of most hydrocarbon fuels [16]. Under this assumption, equation (1) can be written as

$$\tau_l = \tau_g - \gamma(\nabla T)_\theta. \tag{3}$$

Adopting the non-dimensional approach introduced in [11], the above stress balance takes the form

$$\frac{\mu_{l,0}}{\mu_\infty}\tau_l^* = \tau_g^* - \frac{Ma}{a^*}\frac{\partial T^*}{\partial \theta} \tag{4}$$

where the asterisk denotes non-dimensional quantities ($\tau_l^* = \tau_l a_0/(\mu_{l,0} U_\infty)$, $\tau_g^* = \tau_g a_0/(\mu_\infty U_\infty)$, $T^* = T/T_\infty$, $a^* = a/a_0$), and Ma is the Marangoni number defined by $\gamma T_\infty/(U_\infty \mu_\infty)$. The subscript ∞ denotes free-stream conditions, while $\mu_{l,0}$ is the liquid viscosity at injection (time = 0).

The governing equations were solved numerically using an implicit iterative procedure described in [11]. The required computations were very intensive and were performed on a Cray Y-MP supercomputer. A typical run consumed slightly over 3 h of CPU time.

RESULTS AND DISCUSSION

The model produces time-varying spatially-resolved data for the entire flow field within and around the droplet, thus providing information on the fundamental transport processes governing the mass, momentum and energy exchange between the droplet and the gaseous stream. During the initial stages of the current study, it became apparent that the consideration of the Marangoni stress on the gas–liquid interface demands the use of finer grids as compared with the simulations that neglect surface tension gradients [11]. A mesh of 35 (radial direction) × 45 (angular direction) nodes in the gas phase and 60 × 45 nodes in the liquid phase proved to be adequate for grid-independent computations.

All numerical calculations described in the following correspond to an initially quiescent *n*-octane droplet that has a uniform temperature of 300 K before it is suddenly (time = 0) injected into a uniform air stream of temperature 1250 K and pressure 10 atm. The initial Reynolds number (Re_0), as based on droplet diameter, was selected to be 35, 50 or 100. These respective values of Re_0 were chosen by selecting a free-stream velocity of 15 m s^{-1}, and the following droplet diameters; 40, 57 and 113 μm. The above conditions also designate Marangoni numbers that are the same for all three cases; $Ma = 175$. It should be noted here that the Weber numbers corresponding to the droplets with $Re_0 = 35$, 50, 100 are $We = \rho_\infty U_\infty^2 d/\sigma = 1.2$, 1.7 and 3.4, respectively. It is well established that spherical shapes are attainable for $We < 1$, therefore, the above values of We are relatively high for the assumption of sphericity to hold (especially for $Re_0 = 100$). However, the degradation of the efficiency of the employed numerical techniques at lower velocities (which could reduce We below unity) did not allow us to conduct any complete simulations where the assumption of sphericity is entirely consistent with the value of the Weber number. To this end, the reported results for $Re_0 = 35$ and 50 should be representative of slightly deforming droplets, however, the reliability of the model predictions for $Re_0 = 100$ may be questionable.

A comparison is conducted below between the model predictions when the surface tension gradients are taken into account and when they are neglected. The value of $\gamma = 10^{-4}$ N m^{-1}K^{-1} was considered first as representative of liquid hydrocarbon fuels. The temporal scale used in this study has been normalized with respect to the characteristic time for gas-phase hydrodynamic diffusion [$\tau_{Hg} = t\mu_\infty/(\rho_\infty a_0^2)$] according to the formulation followed in [11, 15].

Figure 1 shows the angular variation of droplet surface tangential velocity at various times throughout the base case simulation ($Re_0 = 50$). Note that $\theta = 0°$ corresponds to the front stagnation point of the flow, while $\theta = 180°$ represents the rearmost point of the droplet on the axis of symmetry. In Fig. 1(a), the surface tension gradients have been neglected, while in Fig. 1(b) the Marangoni stresses have been considered on the droplet interface. It is immediately seen that the effect of thermocapillary forces is substantial during the very early stages of the simulations; note the different character of the profiles at $\tau_{Hg} = 0.5$. In fact, the surface fluid motion at that instant is significantly enhanced by the Marangoni forces at the rear of the droplet ($\theta > 120°$). A weaker effect is noticed in this section of the droplet surface after $\tau_{Hg} = 1$. As time proceeds, the familiar bell-shaped angular variation develops [11]. A comparison of Figs. 1(a) and (b) shows that thermocapillary convection enhances the surface tangential velocities at all times. Specifically, almost an 80% increase is noted at $\tau_{Hg} = 5$ when surface-tension gradients are considered. It is noteworthy that the higher interfacial velocities have a far-reaching effect on the fluid dynamics within the droplet interior as will be discussed below.

As seen in Fig. 1, the inclusion of the Marangoni stress in the viscous shear–stress balance on the gas–liquid interface has a positive contribution to the droplet surface tangential velocity, therefore, it enhances liquid motion. A similar trend was reported by Niazmand *et al.* [14] under different ambient conditions; $Re_0 = 10$, $T_\infty = 1000$ K, $p_\infty = 10$ atm. However, their results showed that larger surface tangential velocities lasted for a very short period confined at the beginning of the vaporization history. As reported in [14], after the initial upsurge, the surface tangential velocities were reduced to values much lower than those for a droplet without surface-tension gradient modeling. This trend was attributed [14] to the gradual development of a cool region near the front stagnation point of the flow, which was not verified in the present work.

Figure 2 presents a comparison of the liquid-phase thermal fields at an early stage ($\tau_{Hg} = 1$) of the two simulations ($\gamma = 0$ vs $\gamma = 10^{-4}$ N m^{-1}K^{-1}). The enhancement of the droplet internal motion when thermocapillary forces are modeled is apparent when comparing the two fields. The strong thermocapillary convection in the droplet with $\gamma = 10^{-4}$ N m^{-1}K^{-1} greatly facilitates energy transport from the gas–liquid interface to the droplet interior. Once the internal circulation is established ($\tau_{Hg} > 2$), the isothermal contour patterns for both droplets remain very similar.

Figure 3 shows the angular variations of droplet-

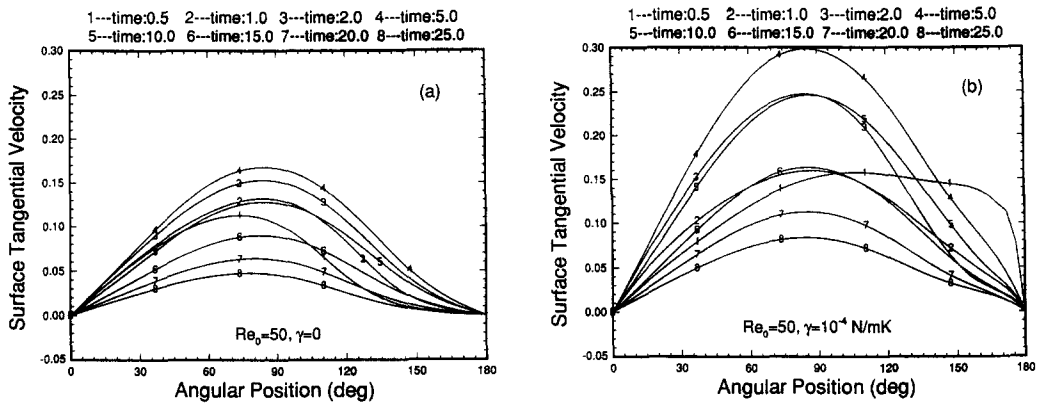

Fig. 1. Angular variation of droplet-surface tangential velocity at various times throughout the base case simulation ($Re_0 = 50$); (a) $\gamma = 0$, (b) $\gamma = 10^{-4}$ N m^{-1}K^{-1}.

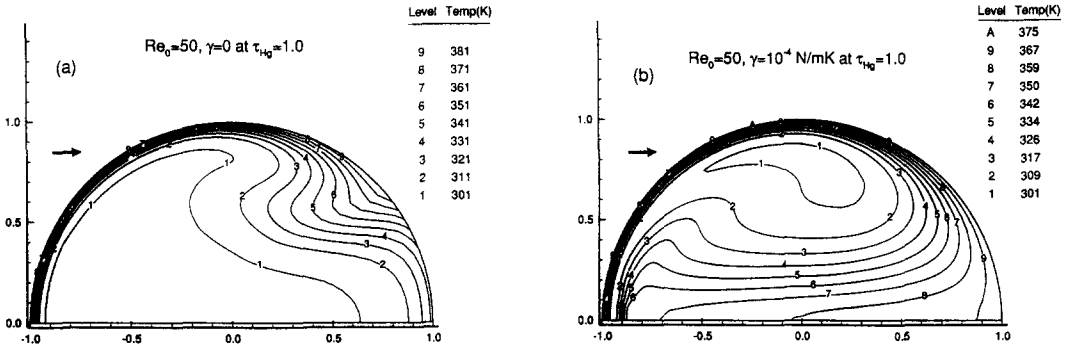

Fig. 2. Comparison of liquid-phase thermal fields at $\tau_{Hg} = 1$ of two simulations with $Re_0 = 50$; (a) $\gamma = 0$, (b) $\gamma = 10^{-4}$ N m^{-1}K^{-1}. The arrows indicate the direction of the ambient gas flow.

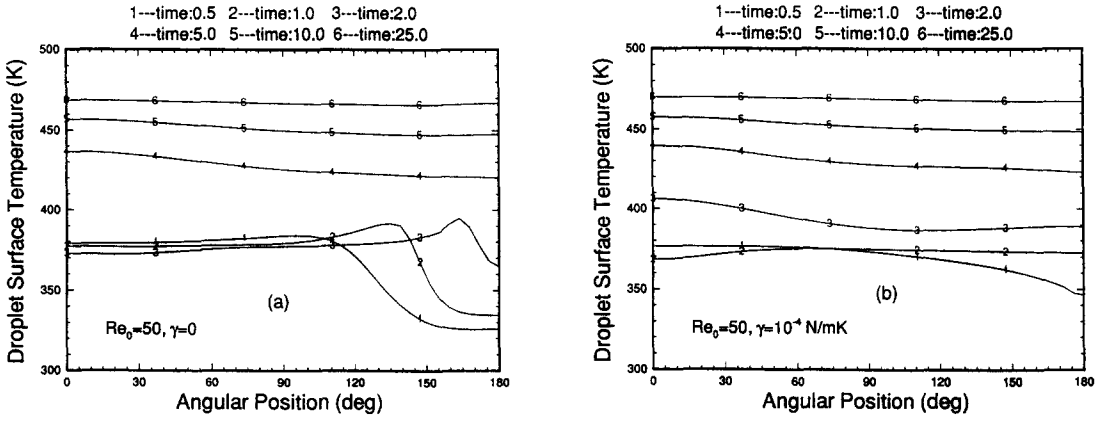

Fig. 3. Angular variation of droplet-surface temperature at various times throughout two simulations with $Re_0 = 50$; (a) $\gamma = 0$, (b) $\gamma = 10^{-4}$ N m^{-1}K^{-1}.

surface temperature at $\tau_{Hg} = 0.5, 1, 2, 5, 10$ and 25 for the two simulations ($\gamma = 0$ vs $\gamma = 10^{-4}$ N m^{-1}K^{-1}). It is noted that at $\tau_{Hg} = 25$ more than 50% of the droplet mass has vaporized. As physically expected, thermocapillary stresses acting along the gas–liquid interface cause a flattening of the $T(\theta)$ profiles [see Fig. 3(b)], thus reducing spatial temperature gradients along the droplet surface. Further comparisons between the liquid-phase thermal fields for $\gamma = 0$ and $\gamma = 10^{-4}$ N m^{-1}K^{-1} showed that the presence of Marangoni stresses also cause a reduction of the temperature gradients along the droplet radius. As a result, the conduction heat transfer is reduced by the Marangoni stresses. However, the convective heat transfer in the droplet interior is enhanced by the higher droplet interface velocities (Fig. 1) corresponding to $\gamma \neq 0$. Figure 3 indicates that the convective heat transfer enhancement ultimately has an overriding influence,

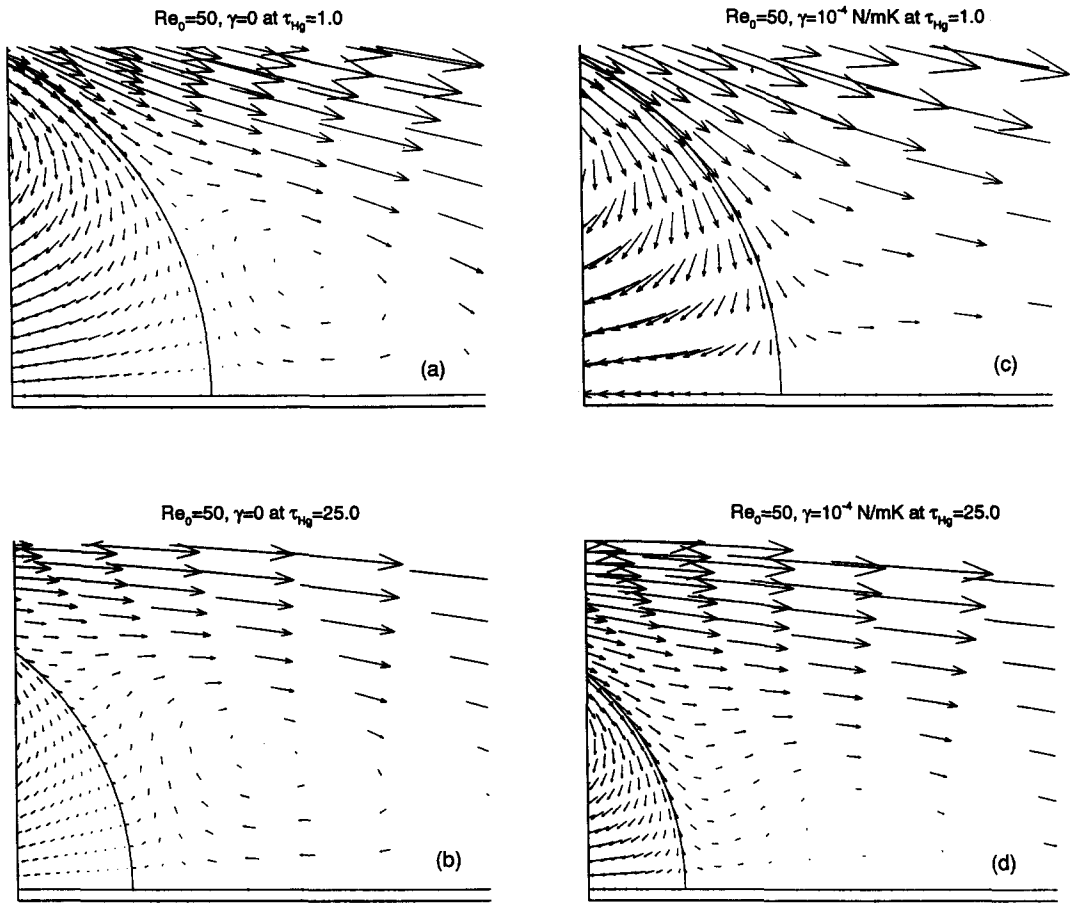

Fig. 4. Side-by-side comparison of the velocity vector fields at two different instants of two simulations with $Re_0 = 50$; (a) $\gamma = 0$, $\tau_{Hg} = 1$, (b) $\gamma = 0$, $\tau_{Hg} = 25$, (c) $\gamma = 10^{-4}$ N m^{-1}K^{-1}, $\tau_{Hg} = 1$, (d) $\gamma = 10^{-4}$ N m^{-1}K^{-1}, $\tau_{Hg} = 25$. Only the rear section of each droplet is shown. The velocity vectors have been plotted with the same length scale.

causing the overall droplet surface temperatures to be slightly higher when Marangoni stresses are present. Although thermocapillary stresses cause a more uniform distribution of heat in the liquid phase, the droplet with $\gamma = 10^{-4}$ N m^{-1}K^{-1} cannot still be characterized as isothermal; for example at $\tau_{Hg} = 25$ the maximum temperature on the droplet surface is 470 K, while the minimum temperature at the center of the toroidal vortex is 464 K. The corresponding temperatures for the droplet with $\gamma = 0$ are 468 K and 457 K, respectively.

Figure 4 presents a side-by-side comparison of the velocity vector fields at two different instants of the two simulations ($\gamma = 0$ vs $\gamma = 10^{-4}$ N m^{-1}K^{-1}). Only the rear section of each droplet is shown in this figure, in which the vectors have been plotted with the same length scale. In contrast to Fig. 4(a), Fig. 4(c) shows no recirculating gaseous wake at $\tau_{Hg} = 1$. The suppression of gaseous recirculation when thermocapillary forces are considered, occurs during the greatest portion of the droplet lifetime and is ascribed to the presence of the surface-tension gradients on the gas–liquid interface. Figures 4(b) and (d) correspond to a later stage ($\tau_{Hg} = 25$) and show the presence of a detached gas-phase recirculation wake for both droplets. The appearance of gas-phase recirculation in Fig. 4(d), though substantially weaker than the one of Fig. 4(b), suggests the reduced thermocapillary effect at late stages of the droplet vaporization lifetime. It is noted that the early suppression of the gaseous recirculation wake by the inclusion of thermocapillary forces in the model was encountered for all three values of Re_0 considered (35, 50, 100).

Figure 5(a) presents the temporal variation of liquid-mass vaporization rate (dimensionless) and surface-averaged temperature for three droplets with $Re_0 = 50$; $\gamma = 0$, 10^{-4} and 2×10^{-4} N m^{-1}K^{-1}. It should be noted that the corresponding values of the Marangoni number for the above cases are 0, 175 and 350. In that respect, Fig. 5 reflects the effect of the Marangoni number on droplet evaporation dynamics. It is seen that the enhanced fluid motion due to thermocapillary forces leads to slightly higher droplet-surface temperatures, and in turn, to higher vaporization rates. This trend contradicts the findings of Niazmand *et al.* [14], who reported higher liquid tem-

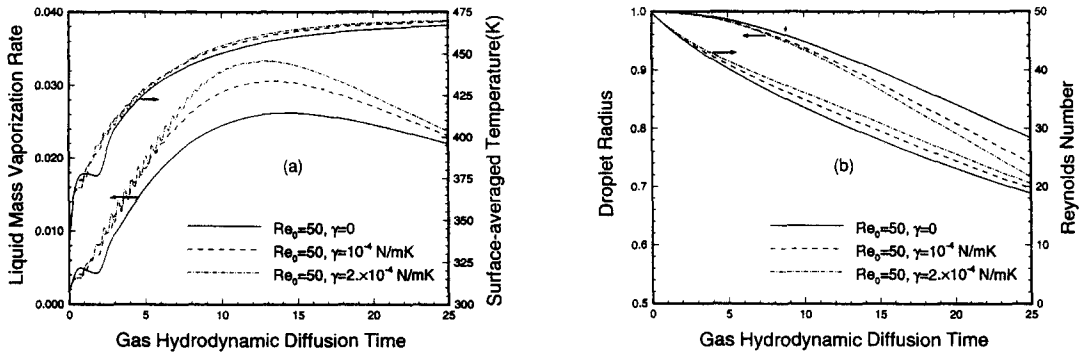

Fig. 5. Temporal variation of (a) liquid mass vaporization rate and surface-averaged temperature, (b) droplet radius and Reynolds number for three droplets with $Re_0 = 50$; $\gamma = 0$, 10^{-4} N m^{-1}K^{-1} and 2×10^{-4} N m^{-1}K^{-1}.

peratures when surface-tension gradients were neglected. The early plateau shown by the solid curves of Fig. 5(a) ($\gamma = 0$) between τ_{Hg} values of 0 and 2 marks the liquid relaxation period after the sudden exposure of the initially quiescent droplet to the gaseous flow [11]. This plateau shrinks appreciably after the inclusion of the Marangoni stresses (dashed curves), probably as a result of the accelerated liquid-phase motion when $\gamma \neq 0$. Figure 5(b) shows the history of droplet radius and Reynolds number for the three $Re_0 = 50$ cases compared; $\gamma = 0$, 10^{-4} and 2×10^{-4} N m^{-1}K^{-1}. As expected, the higher vaporization rates of the droplets with surface-tension gradients yield smaller radii at each instant in time. However, the corresponding instantaneous Reynolds numbers follow an opposite trend, being indicative of higher relative velocities with respect to the free stream when the Marangoni effect is considered. These higher relative velocities, in turn, imply lower drag forces and thus slower droplet deceleration with respect to the gas phase for droplets with $\gamma = -d\sigma/dT \neq 0$.

Figures 6(a)–(d) present the temporal variation of the drag coefficient C_d and its constituent components for three droplets with $Re_0 = 50$; $\gamma = 0$, 10^{-4} and 2×10^{-4} N m^{-1}K^{-1}. The substantially reduced values of C_d for $\gamma \neq 0$ [Fig. 6(a)] are consistent with the temporal variations of the Reynolds numbers shown in Fig. 5(b) and are discussed in the following. The total drag force on each droplet consists of three components [17]: friction drag, pressure drag and thrust drag. The temporal variation of these three quantities is shown in Figs. 6(b)–(d), respectively. As seen in Fig. 6(b), the higher surface tangential velocities and vaporization rates of the droplets with $\gamma \neq 0$ reduce skin friction. Furthermore, Fig. 6(c) shows that the previously discussed suppression of the gas-phase recirculation for $\gamma \neq 0$, reduces the pressure drag component as well. Finally, Fig. 6(d) shows that while the overall contribution of the thrust drag to the value of C_d is relatively low when the thermocapillary stresses are neglected, the corresponding contribution when $\gamma \neq 0$ is appreciably higher due to the stronger angular variation of the evaporation flux from the droplet surface. In fact, the magnitude of the thrust drag component for $\gamma = 10^{-4}$ N m^{-1}K^{-1} is almost double of that for $\gamma = 0$. The combined effect of all three drag components yields a reduced drag when $\gamma \neq 0$, which slows down droplet acceleration. It is noted that all three drag components are affected by the inclusion of the Marangoni stresses, thus emphasizing the complex influence of surface tension gradients on overall droplet evaporation and transport. In response to the weakening character of surface-tension gradients with time, the C_d discrepancy in Fig. 6(a) becomes smaller at late stages of the simulations. It is important to note that higher values of γ have a more dramatic influence on the drag coefficient [compare curves shown in Fig. 6(a)]. In fact, the discrepancy between the values of C_d for $\gamma = 0$ and $\gamma = 2 \times 10^{-4}$ N m^{-1}K^{-1} is as high as 50% at intermediate stages of the droplet lifetime. Finally, the early temporal oscillations of the curves with $\gamma \neq 0$ in Figs. 5(a) and 6(a)–(d) appear to be 'springboarded' by the initial liquid relaxation flow and will be discussed below.

As seen so far, the inclusion of surface tension gradients in the model has an appreciable impact on droplet internal dynamics and drag coefficients. Furthermore, the liquid vaporization characteristics are also influenced by thermocapillary stresses. It is thus expected that the relevant heat and mass transfer numbers are also affected. Figure 7(a) shows the time history of surface-averaged Nusselt numbers for the three droplets with $Re_0 = 50$; $\gamma = 0$, 10^{-4} and 2×10^{-4} N m^{-1}K^{-1}. It is apparent that thermocapillary stresses affect the values of Nu at early stages, while there is little or no effect throughout the latter part of the droplet lifetime. This trend is consistent with the small influence of Marangoni convection on droplet surface temperatures [Fig. 5(a)]. The enhanced liquid motion corresponding to $\gamma \neq 0$ naturally results in higher Nusselt numbers. Figure 7(b) presents the temporal variation of surface-averaged Sherwood numbers for the three droplets considered. It is clear that Marangoni convection appreciably alters the values of Sh through all stages of the droplet lifetimes. The convergence of the three curves at late times is attri-

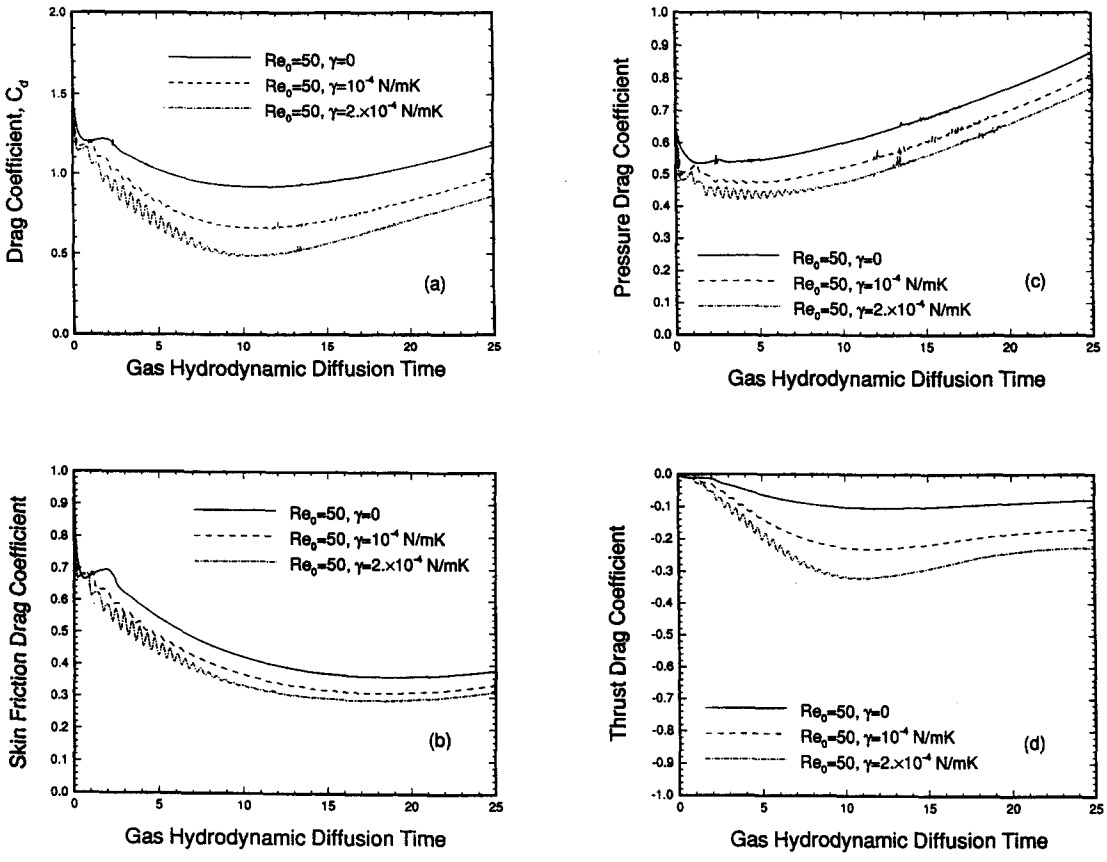

Fig. 6. Temporal variation of drag coefficient C_d and its three components for three droplets with $Re_0 = 50$; $\gamma = 0$, 10^{-4} N m^{-1}K^{-1} and 2×10^{-4} N m^{-1}K^{-1}. (a) C_d, (b) friction drag component, (c) pressure drag component, (d) thrust drag component.

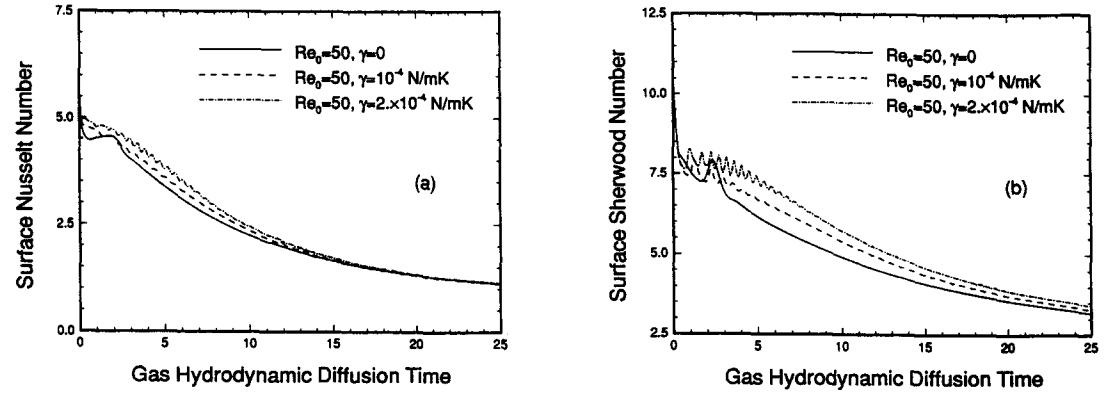

Fig. 7. Time history of (a) surface-averaged Nusselt numbers and (b) surface-averaged Sherwood numbers for three droplets with $Re_0 = 50$; $\gamma = 0$, 10^{-4} N m^{-1}K^{-1} and 2×10^{-4} N m^{-1}K^{-1}.

buted to the timewise attenuation of the surface-tension gradients. It is also noted that the deviations of Nu and Sh are further enhanced by higher values of γ. Finally, all curves corresponding to $\gamma \neq 0$ also display the temporal oscillations that will be discussed in the following.

The importance of thermocapillary effects on the development of the liquid-phase motion, and thus on overall droplet dynamics, can be gauged by comparing the three components of the stress balance on the droplet interface; equation (1). Figures 8(a)–(c) depict a sequence of the angular variation of the three tangential stress components on the droplet surface at three distinct times; $\tau_{Hg} = 1$, 2 and 5. Even though Fig. 8 corresponds to $Re_0 = 50$ and $\gamma = 10^{-4}$ N m^{-1}K^{-1}, the trends shown are representative of other cases as well. It is seen that the magnitude of the Marangoni stress is lower than the two viscous shear

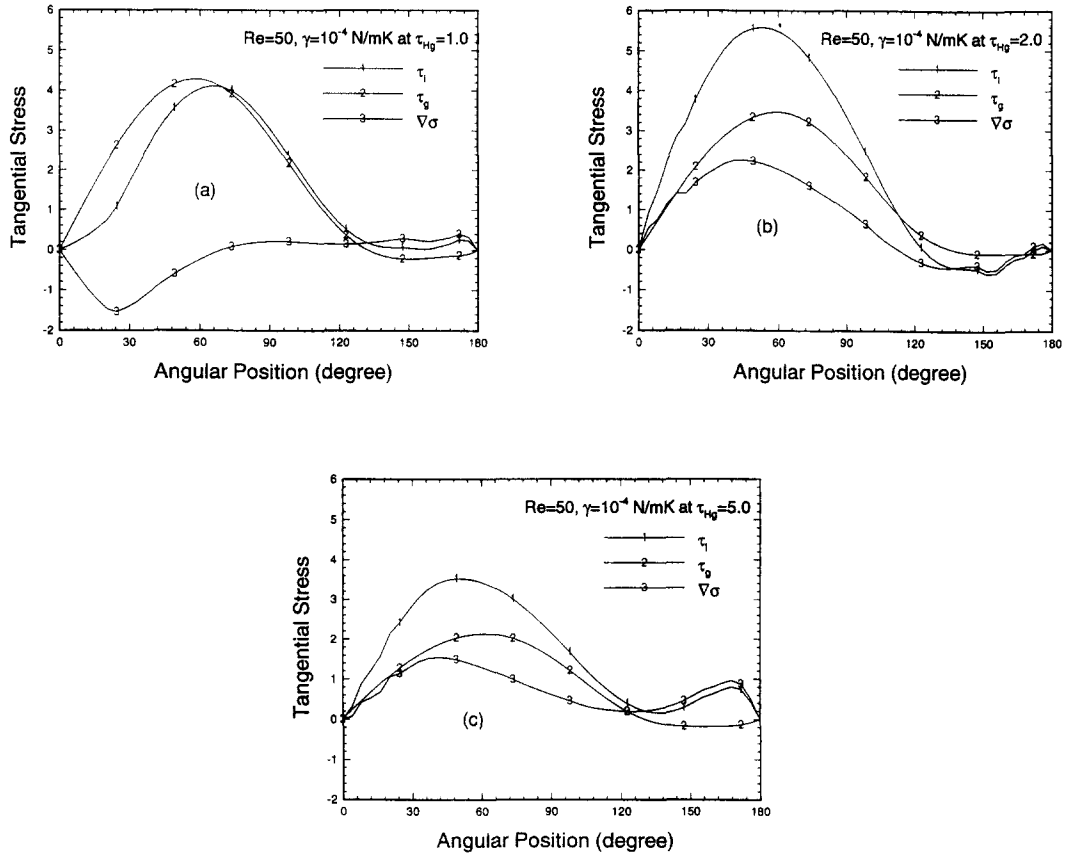

Fig. 8. Angular variation of the three tangential stress components on the droplet surface for $Re_0 = 50$, $\gamma = 10^{-4}$ N m^{-1}K^{-1}; (a) $\tau_{Hg} = 1$, (b) $\tau_{Hg} = 2$ and (c) $\tau_{Hg} = 5$.

components, with the exception of the rear quarter of the droplet surface, where it plays a dominant role at all times. Along the timeline, the distribution of gas phase shear (τ_g) remains coherent and has a diminishing character due to droplet deceleration with respect to the free stream. On the other hand, the Marangoni stress frequently changes direction between $\tau_{Hg} = 0$ and 5. This behavior is due to the changing sign of $\partial T/\partial\theta$ on the droplet surface during that period [see Fig. 3(b)], and influences the temporal dynamic balance of the terms appearing in equation (3). Our simulations clearly showed that the incoherent behavior of the thermocapillary stress is responsible for the early-stage oscillations observed in Figs. 5(a) and 6(a)–(d). From $\tau_{Hg} = 5$ and on, the Marangoni stress distribution maintains a consistent pattern with a decaying behavior. However, the relative importance of the thermocapillary stress remains significant even after $\tau_{Hg} = 10$. To this end, although the tangential temperature gradients on the droplet interface become gradually weaker, their effect on the stress balance is important even at intermediate stages of the droplet lifetime. The sustained influence of the thermocapillary stresses reinforces the shear-induced liquid-phase circulation, and results in significantly enhanced liquid interface velocities throughout the droplet lifetime; Fig. 1.

The above trends regarding the base case simulation ($Re_0 = 50$) were also investigated for $Re_0 = 35$ and 100. As mentioned previously, the different values of Re_0 correspond to the same ambient flow conditions, but different droplet sizes. Therefore, the corresponding values of τ_{Hg} for each instant in time are not identical, but scale according to the inverse square of the droplet radius. The temporal variations of droplet radius for the three values of Re_0 and $\gamma = 0$ or 10^{-4} N m^{-1}K^{-1} are presented in Fig. 9. The enhanced

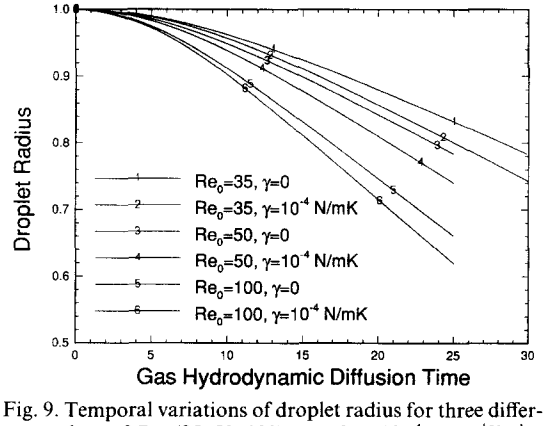

Fig. 9. Temporal variations of droplet radius for three different values of Re_0 (35, 50, 100); $\gamma = 0$ or 10^{-4} N m^{-1}K^{-1}.

liquid evaporation rates corresponding to $\gamma = 10^{-4}$ N m^{-1}K^{-1} are apparent in this figure. It is important to note, however, that the relative effect of thermocapillary stresses on overall droplet evaporation rates appears to be nearly independent of Re_0. This counter-intuitive result was investigated by examining the source of the deviations displayed in Fig. 9 ($\gamma = 0$ vs 10^{-4} N m^{-1}K^{-1}) for each value of Re_0. The relative enhancement of droplet-surface tangential velocities due to the inclusion of the Marangoni stress was found to be very similar in all three Re_0 cases, thus indicating that the relative importance of the surface gradient term in equation (1) is independent of Reynolds number. Finally, it is noted that the early-stage oscillations relevant to surface tension modeling with $Re_0 = 50$ were also encountered for $Re_0 = 35$ and 100.

The origin of the early-stage temporal oscillations depicted in Figs. 5(a), 6 and 7 was examined in this study. As mentioned earlier, these oscillations appear to be 'springboarded' by the liquid relaxation flow after the initial exposure of the droplet to the impulsive ambient motion. The oscillations are pronounced during the early time period, while at later stages they quickly diminish and disappear. It is important to note that the oscillations were absent when surface tension gradients were neglected, therefore, their presence appears to be contingent upon the inclusion of thermocapillary effects in the model. Furthermore, the oscillations consistently showed a grid-independent character, thus verifying that their origin is not numerical. Their magnitude and frequency demonstrated a strong dependence on the value of γ, as seen in Figs. 5(a), 6 and 7. Specifically, the larger the value of γ, the greater the magnitude and the frequency of the oscillations were found to be. Finally, the oscillations of the droplet parameters depicted in Figs. 5(a) and 6 were in phase with the temporal oscillations of the term $(\nabla T)_\theta$ on the droplet surface, as well as the surface tangential velocity, which intimately relates to $(\nabla\sigma)_\theta$. It is worth noting that similar temporal oscillations were reported by Haywood *et al.* [13] who attributed them to the changing droplet shape (the Marangoni effect and droplet deformation were concurrently considered in that study).

Figures 10(a)–(d) present the lifetime history of surface tangential velocity at four specific angular locations on the droplet surface ($\theta = 45$, 90, 135 and 155°) for four different simulations; $Re_0 = 35$, 50, 100 and $\gamma = 10^{-4}$ N m^{-1}K^{-1}, or $Re_0 = 50$ and $\gamma = 2 \times 10^{-4}$ N m^{-1}K^{-1}. The angles θ in the graphs are measured from the front stagnation point ($\theta = 0$). It is emphasized that the temporal scales used in Figs. 10(a)–(c) are not equivalent, since different values of Re_0 correspond to different droplet sizes, which appropriately scale the hydrodynamic diffusion time; $\tau_{Hg} = t\mu_\infty/(\rho_\infty a_0^2)$. For the same reason, the temporal scales of Figs. 10(b) and (d) are equivalent. Consistent with the previous findings, the oscillation is amplified at the rear of each droplet (larger θ) where the Marangoni effect is more effective. It is also important to note that the oscillation frequency for each case is independent of location on the droplet interface (compare curves at $\theta = 135$ and 155°). Even though Figs. 10(a)–(d) show a similar oscillation pattern for different conditions, the corresponding amplitudes are in great disparity. The significantly enhanced amplitude of the oscillations with the value of γ is apparent when comparing Fig. 10(b) ($\gamma = 10^{-4}$ N m^{-1}K^{-1}) with Fig. 10(d) ($\gamma = 2 \times 10^{-4}$ N m^{-1}K^{-1}). The high sensitivity of the oscillation magnitude and frequency on the value of γ confirms the thermocapillary stresses as the source of the oscillations.

The early-stage oscillation frequencies were determined from the temporal variation of surface quantities after a conversion of the abscissa to real time. Table 1 summarizes the frequencies f_C for the droplet simulations considered. The values of f_C show a decreasing trend with rising Re_0. Since different values of Re_0 in this study correspond to different droplet sizes, larger droplets correspond to lower frequencies. Finally, the computed oscillation frequency for $\gamma = 2 \times 10^{-4}$ N m^{-1}K^{-1} was higher compared to the frequency for $\gamma = 10^{-4}$ N m^{-1}K^{-1}.

CONCLUSIONS

The thermocapillary convection effect on the dynamic behavior of a vaporizing–convecting hydrocarbon droplet has been numerically investigated in an axisymmetric flow configuration at ambient pressures and temperatures characteristic of gas-turbine combustor environments. The Reynolds numbers considered were in the range 35–100, as being representative of practical situations of interest.

The model predictions showed that surface-tension gradients due to spatial variations of the temperature along the gas–liquid interface have a profound impact on droplet dynamic behavior. The Marangoni stresses cause a reduction of the temperature gradients not only along the droplet surface, but along the droplet radius as well. The inclusion of the Marangoni stress in the balance of viscous shear stresses on the gas–liquid interface strengthens the droplet-surface tangential velocity, and consequentially enhances the droplet internal circulation. The increased energy transport within droplets in which surface-tension gradients are modeled results in slightly higher droplet-surface temperatures and moderately higher vaporization rates, thus leading to shorter lifetimes when compared to droplets where thermocapillary stresses are neglected. The relative importance of thermocapillary stresses on overall droplet evaporation rates was found to be little affected by Reynolds number.

A significant reduction of drag coefficient was observed when surface-tension gradients along the droplet surface were taken into account. Since smaller drag forces slow down droplet acceleration caused by the gaseous stream, thermocapillary forces are expected to affect droplet transport by ultimately

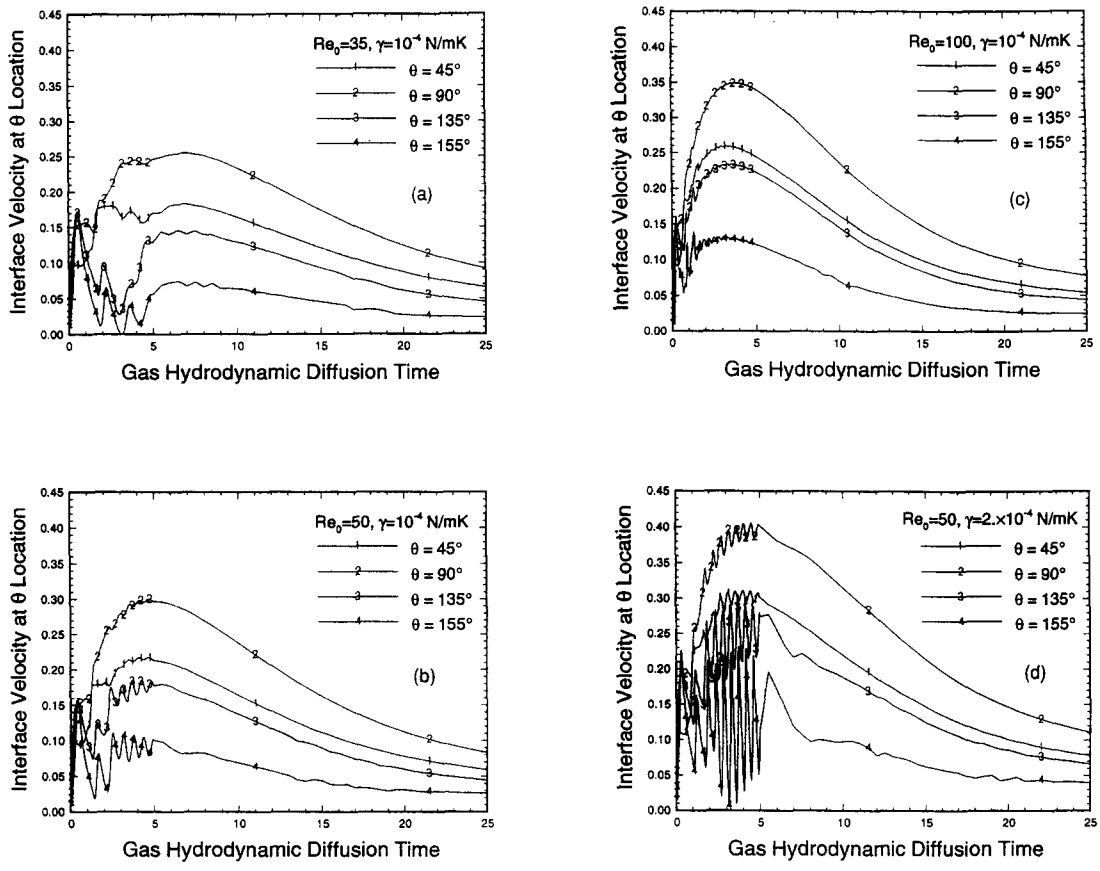

Fig. 10. Lifetime history of surface tangential velocity at four specific angular locations on the droplet surface (θ = 45, 90, 135, 155°) for the simulations listed in Table 1.

Table 1. Computed oscillation frequencies

Case	f_C
$Re_0 = 35, \gamma = 10^{-4}$ N m^{-1}K^{-1}	36 kHz
$Re_0 = 50, \gamma = 10^{-4}$ N m^{-1}K^{-1}	30 kHz
$Re_0 = 100, \gamma = 10^{-4}$ N m^{-1}K^{-1}	18 kHz
$Re_0 = 50, \gamma = 2\times10^{-4}$ N m^{-1}K^{-1}	46 kHz

influencing droplet trajectory. While spatially-averaged Nusselt numbers on the droplet surface were little affected by surface tension gradients, a substantial enhancement of the corresponding Sherwood numbers was predicted in the presence of thermocapillary convection.

The model predictions finally indicated that the Marangoni stresses cause temporal oscillations of the flow along the droplet interface at early stages of the droplet lifetime when temperature gradients are significant. The magnitude and frequency of these oscillations increased with the value of $\gamma = -d\sigma/dT$. Furthermore, the computed oscillation frequencies were found to decrease with increasing Reynolds number.

Acknowledgements—The support of the Pittsburgh Supercomputing Center through an allocation of computer time on the Cray Y-MP is acknowledged with appreciation.

REFERENCES

1. C. K. Law, Recent advances in droplet vaporization and combustion, *Prog. Energy Combust. Sci.* **8,** 171–201 (1982).
2. G. M. Faeth, Evaporation and combustion of sprays, *Prog. Energy Combust. Sci.* **9,** 1–76 (1983).
3. H. A. Dwyer, Calculations of droplet dynamics in high temperature environments, *Prog. Energy Combust. Sci.* **15,** 131–158 (1989).
4. W. A. Sirignano, Fuel droplet vaporization and spray combustion theory, *Prog. Energy Combust. Sci.* **9,** 291–322 (1983).
5. W. A. Sirignano, Fluid dynamics of sprays—1992 Freeman Scholar Lecture, *J. Fluids Engng* **115,** 345–378 (1993).
6. S. Prakash and W. A. Sirignano, Theory of convective droplet vaporization with unsteady heat transfer in the circulating liquid phase, *Int. J. Heat Mass Transfer* **23,** 253–268 (1980).
7. M. Renksizbulut and M. C. Yuen, Numerical study of droplet evaporation in a high-temperature stream, *J. Heat Transfer* **105,** 389–397 (1983).
8. H. A. Dwyer and B. R. Sanders, Detailed computation of unsteady droplet dynamics, *Proceedings of the Twentieth Symposium (International) on Combustion*, pp. 1743–1749. The Combustion Institute, Pittsburgh (1984).
9. M. Renksizbulut and R. J. Haywood, Transient droplet evaporation with variable properties and internal circulation at intermediate Reynolds numbers, *Int. J. Multiphase Flow* **14,** 189–202 (1988).
10. R. J. Haywood, R. Nafziger and M. Renksizbulut, A detailed examination of gas and liquid phase transient

processes in convective droplet evaporation, *J. Heat Transfer* **111**, 495–502 (1989).
11. C. H. Chiang, M. S. Raju and W. A. Sirignano, Numerical analysis of convecting, vaporizing fuel droplet with variable properties, *Int. J. Heat Mass Transfer* **35**, 1307–1324 (1992).
12. D. Lozinski and M. Matalon, Thermocapillary motion in a spinning vaporizing droplet, *Phys. Fluids A* **5**, 1596–1601 (1993).
13. R. J. Haywood, M. Renksizbulut and G. D. Raithby, Transient deformation and evaporation of droplets at intermediate Reynolds numbers, *Int. J. Heat Mass Transfer* **37**, 1401–1409 (1994).
14. H. Niazmand, B. D. Shaw and H. A. Dwyer, Effects of Marangoni convection on transient droplet evaporation at elevated pressures and with negligible buoyancy, 1993 Fall Meeting of the Western States Section of the Combustion Institute, Menlo Park, CA (1993).
15. A. T. Shih and C. M. Megaridis, Finite-difference discretization effects on multidimensional droplet evaporation modeling, *Numer. Heat Transfer A* **25**, 151–169 (1994).
16. N. B. Vargaftik, *Handbook of Physical Properties of Liquids and Gases*, p. 273. Hemisphere, New York (1975).
17. R. Clift, J. R. Grace and M. E. Weber, *Bubbles, Drops and Particles*, p. 178. Academic Press, New York (1978).